HAL open science

# Multiscale framework for rapid change analysis from SAR image time series: Case study of flood monitoring in the central coast regions of Vietnam

Thu Trang Lê, Jean-Luc Froger, Dinh Ho Tong Minh

**To cite this version:**

Thu Trang Lê, Jean-Luc Froger, Dinh Ho Tong Minh. Multiscale framework for rapid change analysis from SAR image time series: Case study of flood monitoring in the central coast regions of Vietnam. Remote Sensing of Environment, 2021, 269, pp.112837. 10.1016/j.rse.2021.112837 . hal-03615218

**HAL Id: hal-03615218**

**https://hal.inrae.fr/hal-03615218v1**

Submitted on 8 Jan 2024

**HAL** is a multi-disciplinary open access archive for the deposit and dissemination of scientific research documents, whether they are published or not. The documents may come from teaching and research institutions in France or abroad, or from public or private research centers.

L'archive ouverte pluridisciplinaire **HAL**, est destinée au dépôt et à la diffusion de documents scientifiques de niveau recherche, publiés ou non, émanant des établissements d'enseignement et de recherche français ou étrangers, des laboratoires publics ou privés.

Distributed under a Creative Commons Attribution - NonCommercial 4.0 International License

Version of Record: https://www.sciencedirect.com/science/article/pii/S0034425721005575
Manuscript_74aac444d462cb074a000ba3d3ebaa10

# Multiscale framework for rapid change analysis from SAR image time series: Case study of flood monitoring in the central coast regions of Vietnam

Thu Trang Lê[a,b,*], Jean-Luc Froger[a,1], Dinh Ho Tong Minh[c]

[a] *Laboratoire Magmas et Volcans (LMV), Université Clermont Auvergne, CNRS, IRD, OPGC, F-63000 Clermont-Ferrand, France*
[b] *Department of Photogrammetry and Remote Sensing, Hanoi University of Mining and Geology (HUMG), 18 Vien Street, 11910 Hanoi, Vietnam*
[c] *Univ Lyon, UJM-Saint-Étienne, UCBL, ENSLyon, CNRS, LGL-TPE UMR5276, F-42023, Saint-Étienne, France*
[d] *Institut National de Recherche en Agriculture, Alimentation et Environnement (INRAE), UMR TETIS, Université de Montpellier, France*

**Abstract**

Recently, the frequency of natural and environmental disasters has increased significantly, causing constant changes on the Earth's surface. Synthetic Aperture Radar (SAR) data have been proved to be useful for operational change monitoring tasks. The multiscale framework presented in this paper aims at detecting and analyzing changes using SAR image time series composed of large-size images. Spatio-temporal changes are initially detected at the subimage scale analysis stage to determine regions and image acquisition dates related to the change occurrence. Detailed changes are then identified at the pixel scale analysis stage between selected acquisitions at each recognized region. This framework was used for flood monitoring over a large area along the central coast of Vietnam (from Thua Thien Hue province to Quang Nam province). We exploited a Sentinel-1 image time series acquired during two rainy seasons and typhoon seasons in the Western Pacific (from September to December of the two years 2017 and 2018). The proposed framework detected flooded areas with a high overall accuracy of 90.4% and could analyze different types of changes that occurred in this time series, i.e. dirac, periodic, chaotic changes, and temporal stability.

*Keywords:* Change analysis; Flood monitoring; Vietnam central coastal regions; SAR image time series; Sentinel-1; Tile-based change detection matrix.



© 2021 published by Elsevier. This manuscript is made available under the CC BY NC user license
https://creativecommons.org/licenses/by-nc/4.0/

## 1. Introduction

The Earth's surface is affected by different natural and environmental disasters, such as volcanic eruptions, earthquakes, tsunamis, floods, deforestations, forest fires, etc. These catastrophic events are also major threats to human life and the world economy (Guo, 2010). The development of Earth observation satellites has allowed the acquisition of a large amount of information about the Earth's surface. Synthetic Aperture Radar (SAR) images, with the independence of light and weather conditions, have been widely exploited as an ideal tool for studying natural hazards and environmental problems (Hu et al. (2016), Mason et al. (2012), Peltier et al. (2017), Belenguer-Plomer et al. (2019), Reiche et al. (2018)). SAR image time series (ITS) densely and regularly provided by new generation satellites (Sentinel-1, for instance) are often large datasets with images of high quality, i.e., high resolution and large coverage (large-size images), short repeat cycles (large number of images) and multipolarization (dual-pol/quad-pol data), that require robust algorithms for big data processing. The temporal evolution analysis of objects of interest from repetitive SAR acquisitions allows natural and environmental hazard characterization (Atzori et al. (2019), Alpers et al. (2017), Giustarini et al. (2015), Le et al. (2019c)), damage assessment (Monti-Guarnieri et al. (2018), Le et al. (2019b)), post-disaster recovery monitoring (Solari et al., 2018), and also the improvement of near-real-time disaster forecasts (e.g., flood forecasts in Hostache et al. (2018)). In this context, the efficient exploitation of information provided by SAR ITS for change and deformation detection and monitoring is, therefore, an attractive issue.

Indeed, diverse approaches to change detection and analysis using SAR ITS have been proposed recently in the literature. Classical detectors based on log-ratio (Rignot and VanZyl, 1993), statistical similarity measure (Inglada and Mercier, 2007) developed

*Corresponding author
*Email addresses:* thu_trang.le@uca.fr (Thu Trang Lê), j-luc.froger@uca.fr (Jean-Luc Froger), dinh.ho-tong-minh@inrae.fr (Dinh Ho Tong Minh)
*Preprint submitted to Elsevier*

for change detection between a pair of SAR images have been extended to multitemporal SAR images for both single- and multi- polarization (Lombardo and Olivier (2001), Quin et al. (2014), Conradsen et al. (2016), Le et al. (2015a), Le et al. (2015b)). Several approaches provide a general view of the temporal variation over observed areas via a symmetric matrix containing change information between all possible image pairs in the time series. In Atto et al. (2013), a Multi-Date Divergence Matrix (MDDM) consisting of dissimilarity between wavelet and curvelet features of each image (or subimage) pair was built for the whole ITS to identify dates when changes occurred. Spatial changes were then detected between images of these dates. The framework proposed in Le et al. (2014) aims at building a Change Detection Matrix (CDM) for each pixel stack of the time series, exhaustively. Changes detected in the CDM are results of similarity tests between every two dates. The NORCAMA (Su et al., 2015) computes a Change Criterion Matrix (CCM) using likelihood ratio test at each pixel position. Then changes detected in CCM are separated into some types by clustering and recognizing classification steps.

In this paper, we focus on the detection of changes induced by flood events. For flood detection and monitoring, *in situ* methods can obtain highly accurate assessments. However, they have limitations due to the high costs of implementation, the dependence on external factors, and the difficulty in undertaking at a large scale (Kussul et al., 2011). Remote sensing based methods (i.e., airborne or spaceborne observations) can deal with large flooded areas for continuous monitoring (Kuenzer et al., 2013). Numerous studies on flood monitoring have used optical data (Ahamed and Bolten (2017), Chignell et al. (2015), Wang et al. (2002),Ticehurst et al. (2014)) and/or SAR data (Amarnath and Rajah (2016), Clement et al. (2018), Boni et al. (2016), Tsyganskaya et al. (2018),Landuyt et al. (2019)). The high cloud cover at flooded areas, particularly in rainy seasons, often obscures the ground observations from optical images. Thus, SAR images are the most suitable data for this task. Overall, among the main algorithms for water detection, such as backscatter based thresholding approaches (Chini et al. (2017), Manjusree et al. (2012), Mason et al. (2014), Martinez and Le-Toan (2007), Martinis et al. (2009)),

classification based approaches (including pixel-based (Chapman et al. (2015), Manjusree et al. (2012)), object-oriented (Martinis et al. (2011), Evans et al. (2010)), region growing (Wan et al. (2019), Marti-Cardona et al. (2013)), and fuzzy classification (Martinis et al. (2015), Twele et al. (2016))), change detection based approaches (Giustarini et al. (2013), Schlaffer et al. (2015), Clement et al. (2018)), the thresholding methods are the most widely used. Based on the backscatter signal, these methods separate a water surface (with low intensities/ amplitudes) from a non-water one (with high intensities/ amplitudes) by using a predefined threshold value. On a scene composed of urban areas and suburbs, the threshold selection is more challenging. In the case of floods, in sparsely populated areas, the backscatter values decrease due to radar returning from water bodies. However, in densely built areas, radar backscatter values increase because of double bounce scattering between buildings and water surface. Therefore, these two areas should be discriminated by user analysis and two different threshold values should be selected. Chini et al. (2019) addressed this issue by taking advantage of the InSAR coherence feature to detect floodwater in urban areas.

In general, almost all recent approaches addressing the Earth surface change detection and analysis using SAR ITS have focused on detecting either spatial changes (Quin et al., 2014) or temporal changes (Colin-Koeniguer et al., 2018). Few approaches have devoted effort to determine both spatial and temporal changes and the analysis of their nature. However, they might not be appropriate when dealing with images covering a large area, but where changes only occur in a small region (Atto et al., 2013), or with a big dataset as they were tested on small ones (Le et al. (2015b), Su et al. (2015)). Therefore, a method is lacking that would exploit the information provided by a long SAR ITS composed of large-size images to identify spatio-temporal changes. In this study, we propose a framework that tackles this issue. The proposed approach is a multiscale processing strategy for a change analysis based on the CDM method (Le et al. (2015b)) suited to handle a long SAR ITS covering a large study area, which was briefly introduced in (Le et al. (2018), Le et al. (2019a)). This work is applied to flood monitoring over a large

area in the central coastal regions of Vietnam using a Sentinel-1 SAR ITS. Flooding is one of the major natural hazards in Vietnam that causes an annual huge loss of life and property. With more than 3200 km long of coastline and 70% of the population living in coastal regions (Bangalore et al., 2019), Vietnam is usually at high risk of flooding due to tropical storms, in particular, at the central coast. The paper is organized as follows: Section 2 describes the study area and the data used for flood monitoring. Section 3 is dedicated to the proposed multiscale framework. Section 4 presents the obtained results and discussion. Finally, conclusions and perspectives are given in section 5.

## 2. Case study and dataset

The coastal region in this study stretches three provinces: Thua Thien Hue, Da Nang and Quang Nam, between $14^o$ 57' N to 16 44' N and $107^o$ 00' E to $108^o$ 44' E (see Fig. 1). The tropical monsoon climate is found in this region. There are two distinct seasons, the dry season from January to August with high temperature, hot and humid climate, and the rainy season from September to December (Matsumoto, 1997). The rainy season coincides with the operation period of typhoons and tropical depressions in the Western Pacific, and the northeast monsoon. Therefore, the rainfall concentrates mainly in this season, accounting for 65% to 80% of the total annual precipitation of the region (Bui, 2011). Due to such weather, floods often occur in this area during the rainy season. According to the reports of the Vietnam Disaster Management Authority, in 2017, the East Sea of Vietnam (the South China Sea) suffered 16 typhoons and 4 tropical depressions, with 7 typhoons directly affecting Vietnam. Natural disasters (i.e., floods, flash floods, and associated landslides) led to 325 deaths; 61 went missing. Total physical damage of US$ 2,567 million has been estimated, the most serious in the last 5 years (vnexpress, 2018). In 2018, 9 typhoons impacted the East Sea of Vietnam, in which 3 ones made landfall in Vietnam. Natural disasters caused 221 deaths and missing people, and an estimated economic loss of US$ 862 million (vnexpress, 2018). In this paper, Sentinel-1 SAR observations of the floods that affected the central coastal regions

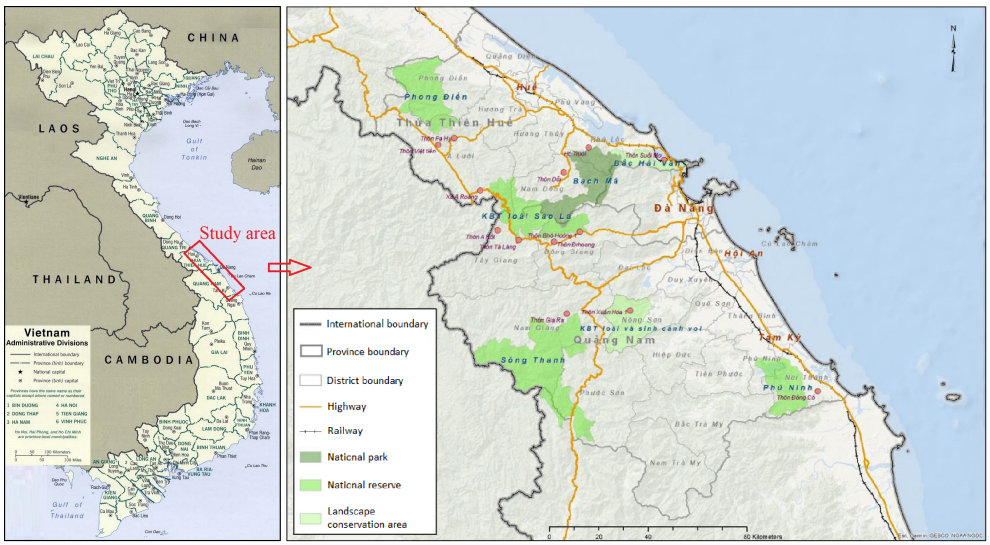


Figure 1: Location of the study area (© University of Texas Libraries (left), and Thua Thien Hue Department of Tourism (right)).

of Vietnam during two rainy seasons in 2017 and 2018 are exploited to apply and validate the proposed method.

The study area during two rainy seasons of the years 2017 and 2018 was under investigation for flood monitoring using a Sentinel-1 C-band SAR ITS. Sentinel-1 is composed of a constellation of two satellites, Sentinel-1A (launched on April 03, 2014) and Sentinel-1B (launched on April 22, 2016), moving on the same orbital plane with $180^o$ phasing apart. Inherited and developed from SAR systems on ERS-1, 2 and Envisat, Sentinel-1 mission provides independent operational capability for medium- to high-resolution radar mapping of the Earth with enhanced temporal resolution, coverage, reliability for applications requiring long time series. The repeat cycle of each Sentinel-1 is 12 days (175 orbits per cycle), so that 6 days for both Sentinel-1A and B. Sentinel-1 SAR sensor operates at C-band frequency (5.405 GHz) and supports operation in single and dual polarizations. Sentinel-1 uses the four observation modes: Stripmap (SM), Interferometric Wide swath (IW), Extra Wide Swath (EW), and Wave. Each mode can produce products at SAR Level-0, Level-1 SLC, Level-1 GRD, and Level-2 OCN.

Table 1: Description of Sentinel-1 data.

| Specifications | Sentinel-1 data |
|---|---|
| Operator | European Space Agency (ESA) |
| Satellite | Sentinel-1A |
| Launched date | April 03, 2014 |
| Satellite orbit | Ascending, track 55 |
| Repeat cycle | 12 days |
| Imaging frequency | C-band at 5.4 GHz |
| Imaging mode | IW |
| Data product | SLC Level-1 |
| Resolution | 3.5 m×22 m (range×azimuth) |
| Pixel spacing | 2.3 m×14.1 m (range×azimuth) |
| Polarization | VV |
| Swath | IW1, IW2 |
| Number of images | 19 images |
| Acquisition dates (YY/MM/DD) | 17/09/11; 17/09/23; 17/10/05; 17/10/29; 17/11/10; 17/11/22; 17/12/04; 17/12/16; 17/12/28; 18/09/06; 18/09/18; 18/09/30; 18/10/12; 18/10/24; 18/11/05; 18/11/17; 18/11/29; 18/12/11; 18/12/23 |

The time series used in this study composed of 19 IW Level-1 Single-Look Complex (SLC) Sentinel-1 images were acquired from the ascending track 55 with a repeat cycle of 12 days, in two periods: from September 11, 2017, to December 28, 2017, and from September 06, 2018, to December 23, 2018. Table 1 summarizes the principal parameters of the dataset used. From such a dataset, we can observe not only the abrupt and cyclical changes caused by floods but also seasonal changes related to aquaculture and agriculture areas. Besides, for the assessment of change detection results, we used a flood map of Thua Thien Hue province regarding the typhoon Damrey in 2017 provided by Brakenridge and Kettner (2017), Dartmouth Flood Observatory at the University of Colorado, from MODIS and Sentinel-1 data (see Fig. 11 a).

## 3. Methods

### *3.1. Data preprocessing*

The Sentinel-1 time series was preprocessed by several steps described in Fig. 2 before applying the proposed framework. We used the Sentinel Application Platform (SNAP), version 6.0, with Graph Processing Tool (GPT) for all preprocessing steps in this study. First, we calibrated acquired SLC Sentinel-1 images so that the radar signal is converted into $\gamma^0$. The radar backscatter $\gamma^0$ best expresses the actual area visible to the radar (in the plane perpendicular to the slant range plane) that can be retrieved (Small, 2011). Then we used the Sentinel-1 TOPS operators to implement the swath and polarization selection and the deburst of Sentinel-1 data, i.e., S-1 TOPS Split, S-1 TOPS Merge, and S-1 TOPS Deburst operators in this paper. Afterward, Sentinel-1 images were multilooked (e.g., four looks in range) to reduce speckle. In our work, no additional speckle filtering is needed to avoid smoothing change information of the time series that can affect the obtained change detection matrix. Finally, all images of the time series were coregistered to stack all pixels associated with the same position on the ground. Besides, we also extracted the subset of the ITS to fit the study area and masked the sea region using the fractional land/water mask processing in SNAP.

### *3.2. Multiscale framework for change analysis*

Let us consider a time series of $N$ cocalibrated and coregistered SAR images sorted by acquisition date $\mathcal{I} = \{\mathcal{I}_t\}_{1 \leqslant t \leqslant N}$, with $\mathcal{I}_t$ the image at time $t$. The framework proposed for rapid analysis of changes from a long SAR ITS made up of large-size images includes two stages of analysis (Fig. 3):

i) subimage scale stage: change regions and image acquisitions of interest (i.e., image acquisition dates related to change events) are quickly detected thanks to CDM approach (Le et al., 2014) at the subimage scale analysis instead of the pixel scale analysis in the original.

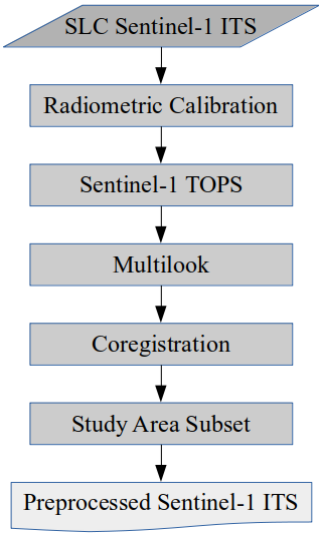


Figure 2: Preprocessing chain for Sentinel-1 image time series.

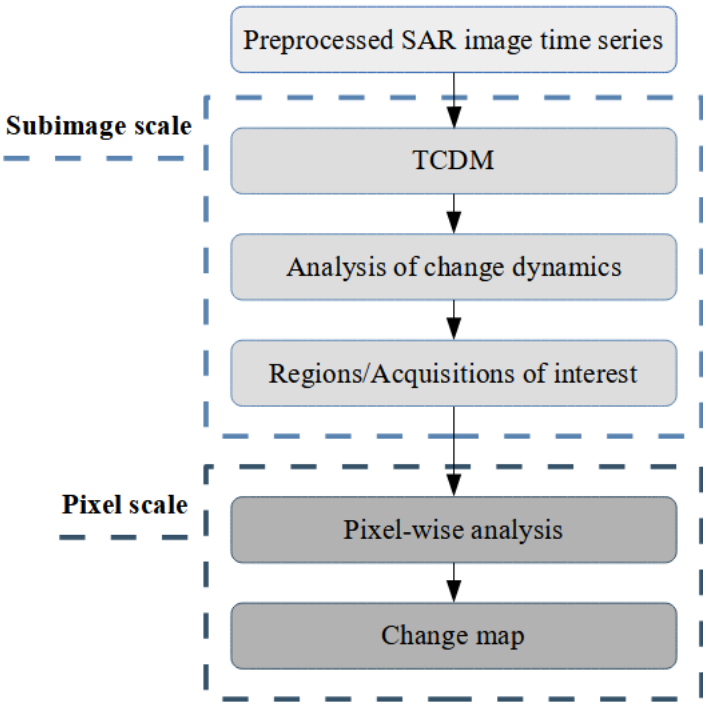


Figure 3: Flowchart of the multiscale change analysis for SAR ITS.

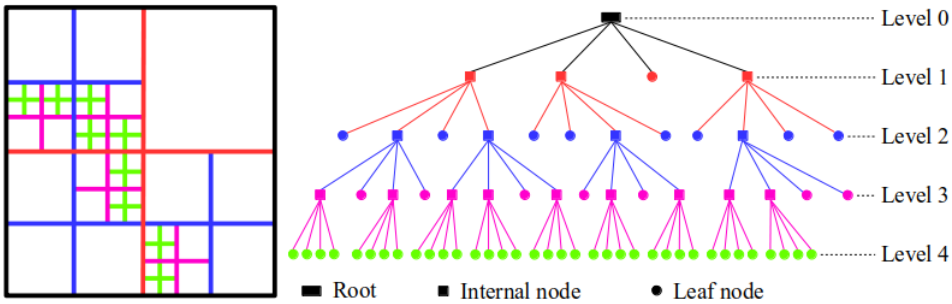


Figure 4: A quadtree with four levels of decomposition.

ii) pixel scale stage: from regions and image acquisitions of interest extracted in the previous stage, detailed changes in these regions are determined.

### *3.2.1. Subimage scale stage*

At this analysis stage, we split each large-size image of the time series into subimages, called tiles, and hence the whole time series is also split into tile stacks. Then we apply the multitemporal change analysis using the CDM approach to each tile stack.

- *Quadtree based - adaptive tile selection*

For SAR image splitting purpose, in Le et al. (2018) and Le et al. (2019a), each image of the time series was divided into tiles of arbitrary size $p \times q$. In Bovolo and Bruzzone (2007), the authors proposed a Split-Based Approach (SBA) for splitting log-ratio SAR images into subimages of the same size, and then they computed threshold values for each subimage based on its statistics. The size of subimages is defined depending on sensor resolution and expected change extension on the ground such that the amount of changed pixels in a subimage is statistically significant for the threshold selection. This approach was also applied in Martinis et al. (2009), Martinis et al. (2015), Pulvirenti et al. (2014). Chini et al. (2017) applied a quadtree decomposition in the approach Hierarchical SBA (HSBA) to split a difference SAR image or single-flood SAR image into subregions with different sizes. With this image splitting, desirable subregions with respect to some statistical characteristics can be selected, for example, subregions showing a bimodal

behavior with two Gaussian balanced populations for threshold determination (Chini et al., 2017). However, SBA and HSBA approaches were proposed for a pair of SAR images or a single image. When applying them to a time series (with the number of images being more than two), if we analyze pairs of images separately, tile sizes of each splitting result will be different, preventing the creation of tile stacks. In this paper, we propose a quadtree based - adaptive tile selection for splitting a SAR ITS into tile stacks.

The quadtree data structure was first introduced in Samet (1984) which refers to a hierarchical set of maximal blocks (tiles) that partition a region (an image). An image is iteratively divided into four equal-sized quadrants, subquadrants. The initial image to be decomposed is the root of the quadtree, and the quadrants (subquadrants) are nodes, including "internal node" with four children and "leaf node" with no children (see Fig. 4 and 5). At each decomposition level, we can test several predefined criteria for each quadrant (e.g., criteria of homogeneity). If the quadrant meets the criteria, it will not be further decomposed, on the opposite, it will be subdivided into four new subquadrants. This procedure finishes whenever every quadrant/ subquadrant meets the criteria or when the size of quadrants reaches the minimum value. The minimum size of quadrants is set such that statistical representativeness is guaranteed. In this paper, we used a variance threshold value ($\lambda$) which is the weighted variance of the whole image $\gamma^0$. If the variance of a quadrant (an image tile) is greater or equal to $\lambda$, the quadrant will be split further. Therefore the image is split sparsely in relatively uniform areas and more intensively where variation is large. This test criterion was applied to each image of the time series to determine the homogeneity of tiles in the quadtree decomposition.

Let $\mathcal{Q}$ denote the quadtree decomposition operator, each image $\mathcal{I}_t$ of the ITS is decomposed into homogeneous tiles of various sizes as follows:

$$\mathcal{I}_t^{\mathcal{S}(i,j,k)} = \mathcal{Q}\left[\mathcal{S}_t(i,j,k)\right](\mathcal{I}_t)\,, \tag{1}$$

where $\mathcal{I}_t^{\mathcal{S}(i,j,k)}$ is an image tile of size $P \times P$ pixels (with $P = 2^{(m-k)}$, $2^m$ and $2^n$ - the maximum and minimum sizes of a tile, respectively) at decomposition level $k$ ($0 \leqslant k \leqslant n$),

$\mathcal{S}_t(i,j,k)$ is the quadtree structure of the decomposed image $\mathcal{I}_t$, and $(i,j)$ is the upper left coordinate of the tile.

The texture varies from one image to another in the time series making the quadtree structures of images different. In order to split the ITS $\{\mathcal{I}_t\}_{1\leqslant t\leqslant N}$ into tile stacks, we took the intersection of all separate quadtree structures and restructured it with respect to maximum and minimum sizes of tiles as the final quadtree structure of the time series $\tilde{\mathcal{S}} = \bigcap_{t=1}^{N} \mathcal{S}_t$. A tile stack of an ITS split by quadtree decomposition is denoted by $\{\mathcal{I}_t^{\tilde{\mathcal{S}}(i,j,k)}\}_{1\leqslant t\leqslant N}$.

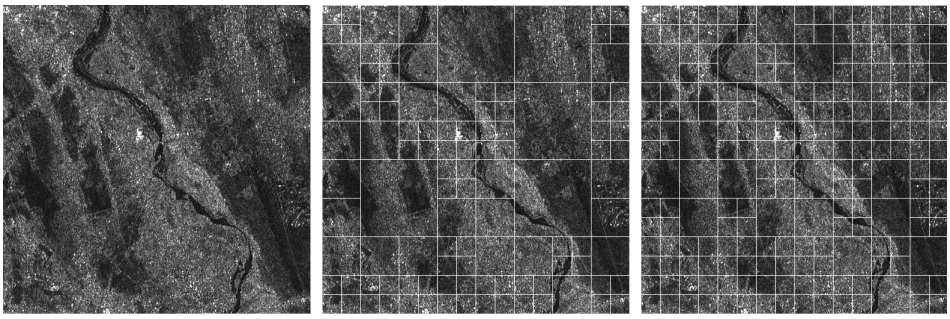

(a) (b) (c)

Figure 5: SAR image split into tiles based on the quadtree decomposition. (a) Sentinel-1 SAR image of Thang Binh district, Quang Nam province, Vietnam, acquired on September 11, 2017, (b) Quadtree-based tiles of the image in Fig. 5a, (c) Final quadtree-based tiles of the time series.

- *Change detection matrix at subimage scale*

We apply the CDM approach to the split ITS for detecting and analyzing changes in each tile stack $(i,j)$ to reduce the computational cost of the pixel-based CDM. A tile-based CDM (TCDM) version constructed by two steps is presented hereafter.

  - Bi-date TCDM: For each tile stack $(i,j)$, we calculate a similarity matrix by taking a similarity measure $\mathfrak{D}$ between each pair of tiles of two different dates $(t,\ell)$ as follows:

$$H_{(t,\ell)}(i,j) = \mathfrak{D}\left(\mathcal{I}_t^{\tilde{\mathcal{S}}(i,j,k)}, \mathcal{I}_\ell^{\tilde{\mathcal{S}}(i,j,k)}\right)_{1\leqslant t,\ell\leqslant N}. \tag{2}$$

The bi-date TCDM $M$ (a binary matrix) is then obtained by comparing values of similarity in $H$ to a threshold $T$ in order to determine changed (denoted as 1) and unchanged (denoted as 0) tiles in the tile stack:

$$M_{(t,\ell)}(i,j) = \left[ H_{(t,\ell)}(i,j) \underset{1}{\overset{0}{\lessgtr}} T \right]. \tag{3}$$

- Multidate TCDM: From the bi-date TCDM, we redefine changed and unchanged tiles using multidate information. To build temporal neighborhoods for each tile $\mathcal{I}_t^{\tilde{S}(i,j,k)}$, unchanged tiles corresponding to date $t$, having the same statistical properties as $\mathcal{I}_t^{\tilde{S}(i,j,k)}$ with respect to $\mathfrak{D}$ and $T$ in the similarity test (3), are aggregated as follows:

$$\Psi\left(\mathcal{I}_t^{\tilde{S}(i,j,k)}\right) = \left\{ \mathcal{I}_\ell^{\tilde{S}(i,j,k)} \mid M_{(t,\ell)}(i,j) = 0 \right\}_{1 \leqslant \ell \leqslant N}. \tag{4}$$

Similar to the previous step, we then compute the multidate TCDM $\hat{M}$ by applying the same similarity measure $\mathfrak{D}$ and a threshold $T$ to temporal neighborhoods of each pair of dates $(t,\ell)$:

$$\hat{H}_{(t,\ell)}(i,j) = \mathfrak{D}\left( \Psi\left(\mathcal{I}_t^{\tilde{S}(i,j,k)}\right), \Psi\left(\mathcal{I}_\ell^{\tilde{S}(i,j,k)}\right) \right)_{1 \leqslant t,\ell \leqslant N}, \tag{5}$$

$$\hat{M}_{(t,\ell)}(i,j) = \left[ \hat{H}_{(t,\ell)}(i,j) \underset{1}{\overset{0}{\lessgtr}} T \right]. \tag{6}$$

The matrix obtained after two steps of temporal change analysis can expose changes occurred over time in each stack. We recall here the characteristic forms of certain types of change (Fig. 6) that can be observed from the appearance of TCDMs (see more details in Le (2015)). Two extreme cases are the temporal stability (Fig. 6 a and b) and the chaotic change (Fig. 6 c and d). The former shows that no changes occurred in the stack, and the latter often describes a rapid surface evolution (e.g., glacier displacement). Two typical change types that can be detected by TCDMs are the dirac (Fig. 6 e and f) and the step changes (Fig. 6 g and h). The dirac change occurs on only one date in the time

series and expresses the behavior of the radiometric temporal signal like a dirac pulse (for instance, a flood event observed on only one date (image)). The step change arises from date $t_k$ and lasts for a certain period or till the end of the time series. This type of change presents an abrupt change (e.g., changes due to natural disasters like volcano eruption, earthquake, etc.). We can also discover more complex change types from the TCDMs. The rampe change in Fig. 6 i and j reports a gradual one with increasing magnitude from date $t_k$ to date $t_\ell$ or till the end of the time series (for example, changes related to cultivated activities, soil/coast erosion). The periodic change in Fig. 6 k and l also shows a gradual change, however, it occurs in a period from date $t_k$ to date $t_\ell$ and repeats cyclically (e.g., seasonal change).

- *Change dynamics of image time series*

Each TCDM contains change information corresponding to a tile stack. By taking into account all "1" elements of a TCDM representing changed tiles, we denote an index of change dynamics that measures the level of change in a tile stack as follows:

$$\delta(i,j) = \frac{2}{N(N-1)} \sum_{t=1}^{N} \sum_{\ell=t+1}^{N} \hat{M}_{(t,\ell)}(i,j). \tag{7}$$

The range of this index is a sequence starting at 0 that indicates the absolute stability, and finishing at 1 that presents the extreme instability of the considered tile stack.

The map of change dynamics of ITS allows us to extract regions of interest from various levels of change. For example, regions with high indexes $\delta$ often show regular changes. But some areas with low indexes $\delta$ may signify changes linked to a specific event. In this paper, we selected regions of interest manually after analyzing the obtained map of change dynamics and TCDMs. However, regions of interest can be identified automatically based on the index of change dynamics. We can select tiles having a specific $\delta$ value or having $\delta$ values within a certain range. The TCDMs in these extracted regions reveal acquisitions of interest associated with change events.

### 3.2.2. Pixel scale stage

After locating regions and image acquisitions of interest, we implement a pixel-wise analysis at these regions between two images acquired on determined dates $(t, \ell)$ to obtain a change map $CM_{(t,\ell)}$:

$$G_{(t,\ell)} = \mathfrak{L}\left(\mathcal{I}_t^{\tilde{S}}, \mathcal{I}_\ell^{\tilde{S}}\right)_{t \neq \ell}, \tag{8}$$

$$CM_{(t,\ell)} = \left[G_{(t,\ell)} \underset{1}{\overset{0}{\lessgtr}} T\right], \tag{9}$$

where $\mathfrak{L}$ measures the similarity degree $G_{(t,\ell)}$ at region $\mathcal{I}^{\tilde{S}}$ between dates $t$ and $\ell$.

It is worth noting that similarity measures $\mathfrak{D}$ and $\mathfrak{L}$ in two stages of the proposed framework can be the same or different. The selection of a similarity measure and a threshold depends on the work scale, data used, for instance, the spatial resolution, the type of SAR data (i.e., single-, multi-polarization SAR, InSAR, etc.), the required accuracy, the cost and time constraints, etc. Several similarity measures for SAR data and automatic thresholding algorithms were reviewed in Le et al. (2015b). In this work, we used the Kullback-Leibler distance (KLD) between two Log-normal distributions (Log-normal KLD) as the similarity measure to identify the difference of shapes of the local probability density functions(PDF) of images in the ITS (Inglada and Mercier, 2007), and the minimum error thresholding (Kittler-Illingworth) method (Kittler and Illingworth, 1986) for the selection of threshold values in all stages of the framework. In Atto et al. (2013), Log-normal KLD is computed as follows:

$$\begin{aligned} KLD_{\text{Logn}}(\mathcal{I}_t, \mathcal{I}_\ell) = & \frac{1}{2}(\alpha_{\mathcal{I}_t} - \alpha_{\mathcal{I}_\ell})^2 \left(\frac{1}{\beta_{\mathcal{I}_t}^2} + \frac{1}{\beta_{\mathcal{I}_\ell}^2}\right) \\ & + \frac{1}{2}\left(\frac{\beta_{\mathcal{I}_\ell}^2}{\beta_{\mathcal{I}_t}^2} + \frac{\beta_{\mathcal{I}_t}^2}{\beta_{\mathcal{I}_\ell}^2}\right) - 1, \end{aligned} \tag{10}$$

with $\alpha$ the log-scale and $\beta$ the shape parameters of probability distributions of the two SAR images $(\mathcal{I}_t, \mathcal{I}_\ell)$ in the comparison.

## 4. Results and discussion

Thanks to the quadtree-based splitting step of the TCDM approach, we only processed 65,640 tile stacks instead of 125,829,120 initial pixel stacks. The TCDM computation time is about 2 hours on an Intel® Xeon® Silver 4110 CPU @ 2.1 GHz, 32 cores with 64 GBytes of RAM. By analyzing TCDMs and map of change dynamics obtained at the subimage scale, we can identify changed regions and image acquisitions of interest. Then we can obtain a detailed change map for each detected region using KLD between selected image pairs at the pixel scale.

### *4.1. Change analysis at subimage scale*

#### *4.1.1. Analysis of change dynamics*

The map of change dynamics in Fig. 7 gives a general view on the behavior and the trend of the variation over time of the observed area at the subimage (tile) scale. Each homogeneous tile of the map has a value that reflects the level of change from 0 to 1. We can see three regions along the coast marked in red rectangles with higher indexes of change dynamics ($0.6 \leq \delta \leq 0.8$) than the others. They are the coasts of Thua Thien Hue province, Da Nang city, and Quang Nam province, respectively. Besides changes due to regular evolution, these areas were also affected by floods occurred during acquisition period. Some small areas marked in white ellipses are lakes and hydropower reservoirs with high indexes $\delta$ due to their water extent changes. Cultivated areas appear on the map with moderate indexes of change dynamics, from 0.3 to 0.5, since the progressive change of crops at these areas was observed during the same growth period of two years (i.e., from September to December of 2017 and 2018). Except for the masked sea area in the upper triangular portion of the map ($\delta = 0$), it could be seen that mountainous areas are quite stable. These areas (almost located in the lower triangular portion of the map) have small $\delta$ values ($0.1 \leq \delta \leq 0.2$). From the map of change dynamics, we selected three regions along the coast marked in red rectangles in Fig. 7, and also lake and reservoir areas for further analysis at the pixel scale.

#### *4.1.2. Analysis of TCDMs*

Fig. 8 shows the TCDMs and temporal profiles of flooded tiles selected in three identified regions of interest. From TCDMs, we detected that in the acquisition period, the study area was affected by three floods observed on November 10, 2017, November 22, 2017, and December 11, 2018 (i.e., the fifth, the sixth, and the eighteenth dates in the time series). On the TCDMs of flooded areas, dirac changed can be determined. The TCDMs reveal that some areas were impacted by only one of three floods (Fig. 8 a, b, c), but some areas were flooded two times (Fig. 8 d, e, f), and even three times (Fig. 8 g) during two rainy seasons of 2017 and 2018. The backscatter mean values of tiles on flood dates are lower than those on other dates (Fig. 8 h, i, j, k, l, m, n). Therefore, the temporal profiles can help us better understand the nature of change types detected by TCDMs. For example, TCDM in Fig. 9 f shows a dirac change detected on November 10, 2017 (the fifth date of the time series) at a mountainous area which looks like a change caused by a flood. However, looking at its temporal profile (Fig. 9 l), the tile backscatter mean value on the fifth date is higher than values on other dates. Thus, this change was not due to a flood but a landslide. Indeed, the typhoon Damrey on November 4, 2017 caused prolonged heavy rains that triggered landslides and flash floods in several mountainous regions in Thua Thien Hue and Quang Nam provinces in the study area. Fig. 9 f, l show the TCDM and temporal profile of a tile selected at Tra My commune, Bac Tra My district, Quang Nam province, where a landslide occurred on November 5, 2017 (TaiNguyenMoiTruong, 2017).

In addition to dirac change at flooded areas, we can also identify other types of change in the study area (see Fig. 9). At rice field areas, periodic change (i.e., seasonal change according to crop evolution) can be observed (Fig. 9 a and c). In the case of flooding, we can see in Fig. 9 a and b that on the fifth, the sixth, and the eighteenth dates of the time series, the rice field area was also flooded like its surrounding areas. And Fig. 9 d shows the opposite case of a rice field stack selected outside of the flooded areas. Aquaculture lagoons along the coast of Thua Thien Hue province (region 1) are covered by water

almost all the time. The backscatter signal at this area changes from one date to another in the time series, therefore its TCDM shows a chaotic change (Fig. 9 e). During the three floods, water overflowed the banks of many lagoons. Therefore, TCDMs observed at regions around these lagoons also present dirac changes as in Fig. 8. As marked in white ellipses in Fig. 7, the study area has many hydropower reservoirs (e.g., Huong Dien, Binh Dien in Thua Thien Hue province, A Vuong, Song Tranh, etc. in Quang Nam province) and lakes (e.g., Khe Ngang, Ta Trach, etc. in Thua Thien Hue province, Hoi Khe, Chua Truoc Dong, etc. in Da Nang city, Khe Tan, Thach Ban, Phu Ninh, etc. in Quang Nam province) and the same phenomenon as the case of aquaculture lagoons can be observed (see Fig. 9 g and h). At almost all lakes and reservoirs, water overflowed their banks during the observed floods. At rocky mountain areas, the TCDM in Fig. 9 i shows temporal stability in the tile stack, consistent with the map of change dynamics.

Thus, from information provided by the map of change dynamics and TCDMs, alongside the analysis of temporal profiles of tile stacks at each specific region, it is possible to preliminarily identify areas affected by floods and acquisition dates of images related to these events. The TCDMs and map of change dynamics are helpful to determine changed regions and images involving these changes, in particular when dealing with a long SAR ITS covering a large area but without additional data sources to get more information about the study area.

#### *4.1.3. Regions and image acquisitions of interest*

The three regions along the coast marked in red rectangles, and several lakes and hydropower reservoirs in Fig. 7 were selected for the pixel scale analysis stage. The first region is the coastal region of Thua Thien Hue province. The second one includes the coastal area of Da Nang city and a small part of Quang Nam province, and zones along two sides of Cam Le river of Da Nang city and Thu Bon river of Quang Nam province. The last one is the rest of the coastal region of Quang Nam province.

As described above, TCDMs disclosed three flooding times observed by the acquired ITS of the study area, i.e., November 10, 2017, November 22, 2017 and December 11, 2018

(the fifth, sixth and eighteenth dates in the time series). Firstly, on November 4, 2017, Damrey - one of the strongest storms hit Vietnam in 2017, caused widespread damage from Thua Thien Hue to Binh Thuan provinces and the Central Highlands. Heavy rain brought by the typhoon the following days caused the first flood. According to the Commanding Committee for Natural Disaster Prevention and Control and Search and Rescue of Thua Thien Hue province, the precipitation from 19:00 November 3, 2017 to 13:00 November 5, 2017 was about 500 to 600 mm at mountainous area. The precipitation was higher than that in some areas, such as 769 mm at Khe Tre, 840 mm at A Luoi, and up to 1,855 mm at Bach Ma (nhandan, 2017). Then, typhoon Kirogi weakened to a tropical depression struck central and southern Vietnam on November 19, 2017. Heavy rain caused the second flood in many parts of this region. In Thua Thien Hue, from 7:00 November 19, 2017 to 19:00 November 20, 2017, precipitation recorded at some stations was: 290 mm at Ho Truoi, 357 mm at Ta Luong, 246 mm at A Luoi, 400 mm at Bach Ma (PCTTTKCN, 2017). Finally, downpours from December 7 to December 10, 2018 induced the third flood in the study site. For example, at some rainfall stations in Hue on December 10, 2018, the precipitation was 513 mm at Phong Binh, 484 mm at Bach Ma, 256 mm at Binh Thanh, 255 mm at Ho Truoi (dantri, 2018). To determine areas affected by each flood in detail, we have chosen the three following image pairs for the calculation of KLD at pixel scale: images acquired on October 29, 2017 (before the first flood) and November 10, 2017 (during the first flood); on October 29, 2017 and November 22, 2017 (before and during the second flood, respectively); and the pair of images acquired on November 29, 2018 and December 11, 2018 (before and during the third flood).

### *4.2. Inundation maps at pixel scale*

The KLD was calculated between three selected pairs of $\gamma^0$ calibrated amplitude images acquired before and during each flood to obtain the similarity maps. The KI thresholding method was then applied to derive change maps (binary change detection results) at each selected region. The obtained change map has the pixel size of 15.5 m x 15.5 m. To better interpret the obtained results, binary change maps of the selected

regions were superimposed on the mean image of the time series and combined in an RGB color image. Fig. 10 shows the inundation maps of three floods during two rainy seasons in 2017 and 2018 of Thua Thien Hue province, Da Nang city, Quang Nam province. We can simultaneously observe the effects of all three floods and identify the frequently flooded areas on these maps. The red, green and blue colors indicate flooded areas induced by the first, the second and the third floods. The yellow, magenta and cyan colors express areas affected by two floods: the first and the second, the first and the third, and the second and the third, respectively. And white color points out areas affected by all three floods.

Specifically, in Thua Thien Hue province, all three floods affected coastal areas, such as Quang Dien, Phu Vang, Phu Loc, Phong Dien, Huong Tra, Huong Thuy districts, and Hue city. In particular, in low-lying regions of Quang Dien, Phong Dien, Huong Tra, and Huong Thuy districts, the damage to cultivation and aquaculture areas was severe. In Da Nang city, the first flood had a minor effect on this city, mainly on one side of Cam Le River. The second and the third affected Cam Le (both sides of the river), some parts of Ngu Hanh Son, Hoa Vang and Hai Chau districts. Like Thua Thien Hue, Quang Nam is also one of the most frequently flooded provinces of Vietnam. We can see that the first flood affected both sides of the Thu Bon river (i.e., Dien Ban, Dai Loc, Duy Xuyen districts), and the coastal regions of Hoi An city, Thang Binh, Phu Ninh and Tam Ky districts. The second one had a smaller impact, mainly in Thang Binh and Phu Ninh districts. And the third one had the most widespread influence of the three floods, in Dien Ban, Duy Xuyen, Hoi An, Thang Binh, Phu Ninh, Tam ky districts. Overall, the inundation map provides a clear view of the frequently flooded areas of the observed region. We can further exploit these maps for the flood-damaged assessment and the flood vulnerability mapping.

### *4.3. Accuracy assessment*

We can observe a relatively high proportion of changed (flooded) pixels at each selected region, suggesting that the proposed TCDM works correctly. Detected inundation

areas are located in low-lying land regions. For a quantitative assessment of obtained change detection results, we used comparison samples extracted based on the flood map on November 7, 2017, derived from MODIS and Sentinel-1 data over Thua Thien Hue province (see Fig. 11 b) to compare to the flood map obtained by the proposed framework on November 10, 2017 (the first flood). We adopted the following evaluation metrics to measure the limited errors, i.e., False Alarm (FA), Missed Alarm (MA), and Overall Error (OE). We also used the Critical Success Index (CSI) (Schaefer, 1990) to assess the obtained binary change map. CSI combines the FA and MA into one score and does not consider the nonflooded fraction within the test-site. This index ranges from $[0, 1]$, the higher values indicating the better performance of the change detection operator. These metrics are calculated as follows:

$$\begin{aligned} FA &= 1 - \frac{TP}{TP + FP}, \\ MA &= 1 - \frac{TP}{TP + FN}, \\ OE &= 1 - \frac{TP + TN}{TP + FP + FN + TN}, \\ CSI &= \frac{TP}{TP + FP + FN}. \end{aligned} \tag{11}$$

where $TP, FP, TN, FN$ are true positive, false positive, true negative, and false negative, respectively, in the confusion matrix (Table 2).

Among the total of 13891 comparison samples, the change map has 6405 correct and 166 false changed pixels, while 1165 changed pixels are misclassified into unchanged class. Accordingly, limited errors are 9.6% of OE, 2.5% of FA, and 15,4% of MA. The obtained change detection result has overall accuracy of 90.4% and the CSI of 82.8%. We can see that the flood detection results of the two maps in Fig 11 are quite consistent, with few false alarms. The comparison map reports the flooding state on November 7, 2017, whilst the flood map produced in this paper describes the state on November 10, 2017, resulting in changes in the flood delineation between the two maps that might explain false alarms.

Table 2: Confusion matrix of change detection result.

| Class | | Validation samples | | Total |
|---|---|---|---|---|
| | | Changed | Unchanged | |
| Change map | Changed | 6405 | 166 | 6571 |
| | Unchanged | 1165 | 6155 | 7320 |
| Total | | 7570 | 6321 | 13891 |

## 5. Conclusions

In this study, we have developed a methodology for a multiscale change analysis from a long SAR image time series composed of large-size image. We proposed to use a quadtree decomposition to split the ITS into tile stacks, and then apply the CDM approach to these stacks for change analysis at the subimage scale. The proposed TCDM approach allows the fast and correct detection of regions and image acquisitions of interest (i.e., changed areas and acquisition dates of images involving change events). Then we derived detailed change maps of detected regions between image acquisitions of interest at the pixel scale. In order to better interpret, the obtained change maps were combined in an RGB color image.

The proposed framework was successfully applied to monitor inundation areas along the coastal regions of Thua Thien Hue, Da Nang and Quang Nam provinces of Vietnam by using a SAR ITS composed of 19 ascending Sentinel-1 images. Obtained TCDMs were capable of identifying different kinds of change in this time series (i.e., dirac change, periodic change, chaotic change, and temporal stability). The results indicate that during two rainy seasons from September to December of the two years 2017 and 2018, the coastal regions from Thua Thien Hue to Quang Nam suffered three floods observed by images acquired on November 10 and 22, 2017, and on December 11, 2018. Most of the coastal districts of these provinces were affected, some of them were seriously flooded, such as Phong Dien, Huong Tra, Phu Vang, etc., of Thua Thien Hue, Hoa Vang, Cam le of Da Nang, and Dien Ban, Dai Loc, Duy Xuyen, Thang Binh, Phu Ninh, etc., of Quang Nam. The established inundation map has the potential to be exploited in further tasks

like flood-damaged assessment, and spatial prediction of flood-susceptible areas.

For further applications of the proposed framework, when using SAR data of different sensors covering different regions, an appropriate similarity measure should be used to fit the size of split tiles. With sensors of low or medium resolution, we can use a similarity measure between tiles containing a large number of samples to detect changes in the study area (e.g., the KLD in this paper). With high resolution ones, a similarity measure between tiles of small neighborhoods (like the coefficient of variation) can be used to preserve the details of high resolution data. The TCDM analysis shows that many kinds of change can be detected by TCDMs. Change detection results of the proposed framework are expected to be classified into different types of landcover change based on TCDMs, and improved by using global terrain data.

## Acknowledgment

This research was financed by the French government IDEX-ISITE initiative 16-IDEX-0001 (CAP 20-25).

## References

Ahamed, A., Bolten, D., 2017. A modis-based automated flood monitoring system for southeast asia. International Journal of Applied Earth Observation and Geoinformation 61, 104–117.

Alpers, W., Holt, B., Zeng, K., 2017. Oil spill detection by imaging radars: Challenges and pitfalls. Remote Sensing of Environment 201, 133–147.

Amarnath, G., Rajah, A., 2016. An evaluation of flood inundation mapping from modis and alos satellites for pakistan. Geomatics, Natural Hazards and Risk 7, 1526–1537.

Atto, A. M., Trouve, E., Berthoumieu, Y., Mercier, G., 2013. Multidate divergence matrices for the analysis of SAR image time series. IEEE Trans. Geosci. Remote Sens. 51, no. 4, 1922–1938.

Atzori, S., Antonioli, A., C.Tolomei, Novellis, V. D., Luca, C. D., Monterroso, F., 2019. Insar full-resolution analysis of the 2017-2018 m>6 earthquakes in mexico. Remote Sensing of Environment 234.

Bangalore, M., Smith, A., Veldkamp, T., 2019. Exposure to floods, climate change, and poverty in Vietnam. Economics of Disasters and Climate Change 3, 79–99.

Belenguer-Plomer, M., Tanase, M., Fernandez-Carrillo, A., Chuvieco, E., 2019. Burned area detection and mapping using sentinel-1 backscatter coefficient and thermal anomalies. Remote Sens. Environ. 233, 1–18.

Boni, G., Ferraris, L., Pulvirenti, L., Squicciarino, G., Pierdicca, N., Candela, L., Pisani, A. R., Zoffoli, S., Onori, R., Proietti, C., Pagliara, P., 2016. A prototype system for flood monitoring based on flood forecast combined with cosmo-skymed and sentinel-1 data. IEEE Journal of Selected Topics in Applied Earth Observations and Remote Sensing 9 (6), 2794–2805.

Bovolo, F., Bruzzone, L., 2007. A split-based approach to unsupervised change detection in large-size multitemporal images: Application to tsunami-damage assessment. IEEE Trans. Geosci. Remote Sens. 45, no. 6, 1658–1670.

Brakenridge, G. R., Kettner, A. J., 2017. Dfo flood event 4533. Dartmouth Flood Observatory, University of Colorado, Boulder, Colorado, USA.
URL https://floodobservatory.colorado.edu/Events/2017Vietnam4533/2017Vietnam4533.html

Bui, V. C., 2011. Forecast of coastal floods in the southern central region in the context of climate change and sea level rise. Tech. rep., Hydrometeorological Station of the South Central Region, Department of Meteorology, Hydrology and Climate Change of Vietnam.

Chapman, B., McDonald, K., Shimada, M., Rosenqvist, A., Schroeder, R., Hess, L., 2015. Mapping regional inundation with spaceborne l-band sar. Remote Sensing 7, 5440–5470.

Chignell, S. M., Anderson, R. S., Evangelista, P. H., Laituri, M. J., Merritt, D. M., 2015. Multi-temporal independent component analysis and landsat 8 for delineating maximum extent of the 2013 colorado front range flood. Remote Sensing 7, 9822–9843.

Chini, M., Hostache, R., Giustarini, L., Matgen, P., 2017. A hierarchical split-based approach for parametric thresholding of sar images: Flood inundation as a test case. IEEE Transactions on Geoscience and Remote Sensing 55, 6975–6988.

Chini, M., Pelich, R., Pulvirenti, L., Pierdicca, N., Hostache, R., Matgen, P., 2019. Sentinel-1 insar coherence to detect floodwater in urban areas: Houston and hurricane harvey as a test case. Remote Sensing 11, 107.

Clement, M. A., Kilsby, C. G., Moore, P., 2018. Multi-temporal synthetic aperture radar flood mapping using change detection. Journal of Flood Risk Management 11, 152–168.

Colin-Koeniguer, E., Boulch, A., Trouve-Peloux, P., 2018. Colored visualization of multitemporal SAR data for change detection: issues and methods. In: In the proceedings of EUSAR 2018 - 12th European Conference on Synthetic Aperture Radar.

Conradsen, K., Nielsen, A. A., Skriver, H., 2016. Determining the points of change in time series of polarimetric sar data. Transaction on Geoscience and Remote Sensing 54, 3007–3024.

dantri, 2018. Hue nguy co ngap sau, mua cang luc cang lon. Available online: https://dantri.com.vn/xa-

hoi/hue-nguy-co-ngap-sau-mua-cang-luc-cang-lon-20181210164054075.htm (accessed on november 10, 2021).

Evans, T. L., Costa, M., Telmer, K., Silva, T. S. F., 2010. Using alos/palsar and radarsat-2 to map land cover and seasonal inundation in the brazilian pantanal. IEEE Journal of Selected Topics in Applied Earth Observations and Remote Sensing 3, 560–575.

Giustarini, L., Chini, M., Hostache, R., Pappenberger, F., Matgen, P., 2015. Flood hazard mapping combining hydrodynamic modeling and multi annual remote sensing data. Remote Sensing 7, 14200–14226.

Giustarini, L., Hostache, R., Matgen, P., Schumann, G. J. P., Bates, P. D., Mason, D. C., 2013. A change detection approach to flood mapping in urban areas using terrasar-x. IEEE Transactions on Geoscience and Remote Sensing 51, 2417–2430.

Guo, H., 2010. Understanding global natural disasters and the role of earth observation. International Journal of Digital Earth 3, 221–230.

Hostache, R., Chini, M., Giustarini, L., Neal, J., Kavetski, D., Wood, M., Corato, G., Pelich, R. M., Matgen, P., 2018. Near-real-time assimilation of SAR derived flood maps for improving flood forecasts. Water Resources Research 54, 5516–5535.

Hu, X., Wang, T., Pierson, T. C., Lu, Z., Kim, J. W., Cecere, T. H., 2016. Detecting seasonal landslide movement within the cascade landslide complex (washington) using time-series sar imagery. Remote Sensing of Environment 187, 49–61.

Inglada, J., Mercier, G., 2007. A new statistical similarity measure for change detection in multitemporal SAR images and its extension to multiscale change analysis. IEEE Trans. Geosci. Remote Sens. 45, no. 5, 1432–1445.

Kittler, J., Illingworth, J., 1986. Minimum error thresholding. Patten Recognition 19, No. 1, 41–47.

Kuenzer, C., Guo, H., Huth, J., Leinenkugel, P., Li, X., Dech, S., 2013. Flood mapping and flood dynamics of the mekong delta: Envisat-asar-wsm based time series analyses. Remote Sensing 5, 687–715.

Kussul, N., Shelestov, A., Skakun, S., 2011. Flood Monitoring from SAR Data. Springer: Heidelberg, Germany, pp. 19–29.

Landuyt, L., Van Wesemael, A., Schumann, G. J.-P., Hostache, R., Verhoest, N. E. C., Van Coillie, F. M. B., 2019. Flood mapping based on synthetic aperture radar: An assessment of established approaches. IEEE Trans. Geosci. Remote Sens. 57, 722–739.

Le, T. T., 2015. Change information extraction from synthetic aperture radar image time series. Ph.D. thesis.

Le, T. T., Atto, A. M., Trouve, E., 2015a. Change analysis using multitemporal SENTINEL-1 SAR images. in Proc. IGARSS Milan, Italy, 4145–4148.

Le, T. T., Atto, A. M., Trouve, E., Nicolas, J. M., 2014. Adaptive multitemporal SAR image filtering based on the change detection matrix. IEEE Geosci. Remote Sens. Lett. 11, no. 10, 1826–1830.

Le, T. T., Atto, A. M., Trouve, E., Solikhin, A., Pinel, V., 2015b. Change detection matrix for multitemporal filtering and change analysis of SAR and PolSAR image time series. ISPRS J. Photogramm. Remote Sens. 107, 64–76.

Le, T. T., Froger, J. L., Hrysiewicz, A., 2019a. Multiscale change analysis for sar image time series: Application to inundation detection. In: IEEE International Geoscience and Remote Sensing Symposium (IGARSS), Yokohama, Japan.

Le, T. T., Froger, J.-L., Hrysiewicz, A., Paris, R., 2019b. Coherence change analysis for multipass insar images based on the change detection matrix. In: IEEE International Geoscience and Remote Sensing Symposium (IGARSS), Yokohama, Japan.

Le, T. T., Froger, J.-L., Hrysiewicz, A., Pham, H. T., 2019c. Multitemporal insar coherence change analysis: Application to volcanic eruption monitoring. In: 10th International Workshop on the Analysis of Multitemporal Remote Sensing Images (MultiTemp), Shanghai, China.

Le, T. T., Tran, V. A., Pham, H. T., Tran, X. T., 2018. Change detection in multitemporal sar images using a strategy of multistage analysis. In: Tien Bui D., Ngoc Do A., Bui HB., Hoang ND. (eds) Advances and Applications in Geospatial Technology and Earth Resources. GTER 2017. Springer, Cham, 152–165.

Lombardo, P., Olivier, C. J., 2001. Maximum likelihood approach to the detection of changes between multitemporal SAR images. IEEE Proc. Radar, Sonar Navig 148, no. 4.

Manjusree, P., Kumar, L. P., Bhatt, C. M., Rao, G. S., Bhanumurthy, V., 2012. Optimization of threshold ranges for rapid flood inundation mapping by evaluating backscatter profiles of high incidence angle sar images. International Journal of Disaster Risk Science 3, 113–122.

Marti-Cardona, B., Dolz-Ripolles, J., Lopez-Martinez, C., 2013. Wetland inundation monitoring by the synergistic use of envisat/asar imagery and ancilliary spatial data. Remote Sensing of Environment 139, 171–184.

Martinez, J. M., Le-Toan, T., 2007. Mapping of flood dynamics and spatial distribution of vegetation in the amazon floodplain using multitemporal sar data. Remote sensing of Environment 108, 209–223.

Martinis, S., Kersten, J., Twele, A., 2015. A fully automated terrasar-x based flood service. ISPRS Journal of Photogrammetry and Remote Sensing 104, 203–212.

Martinis, S., Twele, A., Voigt, S., 2009. Towards operational near real-time flood detection using a split-based automatic thresholding procedure on high resolution terrasar-x data. Natural Hazards and Earth System Sciences 9, 303–314.

Martinis, S., Twele, A., Voigt, S., 2011. Unsupervised extraction of flood-induced backscatter changes in sar data using markov image modeling on irregular graphs. IEEE Transactions on Geoscience and

Remote Sensing 49, 251–263.

Mason, D. C., Giustarini, L., Garcia-Pintado, J., Cloke, H. L., 2014. Detection of flooded urban areas in high resolution synthetic aperture radar images using double scattering. International Journal of Applied Earth Observation and Geoinformation 28, 150–159.

Mason, D. C., Schumann, G. J.-P., Neal, J. C., Garcia-Pintado, J., Bates, P. D., 2012. Automatic near real-time selection of flood water levels from high resolution synthetic aperture radar images for assimilation into hydraulic models: A case study. Remote Sensing of Environment 124, 705–716.

Matsumoto, J., 1997. Seasonal transition of summer rainy season over indochina and adjacent monsoon region. Advances in Atmospheric Sciences 14, 231–245.

Monti-Guarnieri, A. V., Brovelli, M. A., Manzoni, M., Mariotti d'Alessandro, M., Molinari, M. E., Oxoli, D., 2018. Coherent change detection for multipass sar. IEEE Transactions on Geoscience and Remote Sensing 56 (11), 6811–6822.

nhandan, 2017. Thua thien - hue: Mua lon, nhieu noi chim trong bien nuoc. https://nhandan.vn/tin-tuc-xa-hoi/thua-thien-hue-mua-lon-nhieu-noi-chim-trong-bien-nuoc-308507/ (accessed on november 10, 2021).

PCTTTKCN, 2017. Bao cao nhanh: Tinh hinh dien bien va cong tac trien khai ung pho voi mua lu. URL http://pclb.thuathienhue.gov.vn/Portals/0/Bao%20cao%20nhanh%20245%20luc%2019h%20ngay%2020%20thang%2011.doc

Peltier, A., Froger, J.-L., Villeneuve, N., Catry, T., 2017. Assessing the reliability and consistency of InSAR and GNSS data for retrieving 3D-displacement rapid changes, the example of the 2015 Piton de la Fournaise eruptions. Journal of Volcanology and Geothermal Research 344 (15), 106–120.

Pulvirenti, L., Marzano, F. S., Pierdicca, N., Mori, S., Chini, M., 2014. Discrimination of water surfaces, heavy rainfall, and wet snow using cosmo-skymed observations of severe weather events. IEEE Transactions on Geoscience and Remote Sensing 52, 858–869.

Quin, G., Pinel-Puyssegur, B., Nicolas, J.-M., Loreaux, P., 2014. MIMOSA: An automatic change detection method for SAR time series. IEEE Trans. Geosci. Remote Sens 52, no. 9, 5349–5363.

Reiche, J., Hamunyela, E., Verbesselt, J., Hoekman, D., Herold, M., 2018. Improving near-real time deforestation monitoring in tropical dry forests by combining dense sentinel-1 time series with landsat and alos-2 palsar-2. Remote Sensing of Environment 204, 147–161.

Rignot, E. J. M., VanZyl, J. J., 1993. Change detection techniques for ERS 1 SAR data. IEEE Trans. Geosci. Remote Sens. 31, no. 4, 896–906.

Samet, H., 1984. The quadtree and related hierarchical data structures. ACM Computing Surveys 16, 187–260.

Schaefer, J. T., 1990. The critical success index as an indicator of warning skill. Weather and Forecasting 5, 570–575.

Schlaffer, S., Matgen, P., Hollaus, M., Wagner, W., 2015. Flood detection from multi-temporal sar data using harmonic analysis and change detection. International Journal of Applied Earth Observation and Geoinformation 38, 15–24.

Small, D., 2011. Flattening Gamma: Radiometric terrain correction for SAR imagery. IEEE Trans. Geosci. Remote Sens. 49, 3081–3093.

Solari, L., Barra, A., Herrera, G., Bianchini, S., Monserrat, O., Bejar-Pizarro, M., Crosetto, M., Sarro, R., Moretti, S., 2018. Fast detection of ground motions on vulnerable elements using sentinel-1 insar data. Geomatics, Natural Hazards and Risk 9 (1), 152–174.

Su, X., Deledalle, C. A., Tupin, F., Sun, H., 2015. NORCAMA: Change analysis in sar time series by likelihood ratio change matrix clustering. ISPRS Journal of Photogrammetry and Remote Sensing 101, 247–261.

TaiNguyenMoiTruong, 2017. Quang nam: Sat lo nui vui lap 7 nguoi o bac tra my. Available online: https://baotainguyenmoitruong.vn/quang-nam-sat-lo-nui-vui-lap-7-nguoi-o-bac-tra-my-286270.html (accessed on november 10, 2021).

Ticehurst, C., Guerschman, J. P., Chen, Y., 2014. The strengths and limitations in using the daily modis open water likelihood algorithm for identifying flood events. Remote Sensing 6, 11791–11809.

Tsyganskaya, V., Martinis, S., Marzahn, P., Ludwig, R., 2018. Detection of temporary flooded vegetation using sentinel-1 time series data. Remote Sensing 10, 1286.

Twele, A., Cao, W., Plank, S., Martinis, S., 2016. Sentinel-1-based flood mapping: a fully automated processing chain. Internatinal of Remote Sensing 37, 2990–3004.

vnexpress, 2018. Thien tai lam hon 200 nguoi chet, thiet hai 20.000 ty dong. Available online: https://vnexpress.net/thoi-su/thien-tai-lam-hon-200-nguoi-chet-thiet-hai-20-000-ty-dong-3861837.html (accessed on november 14, 2019).

Wan, L., Liu, M., Wang, F., Zhang, T., You, H. J., 2019. Automatic extraction of flood inundation areas from sar images: a case study of jilin, china during the 2017 flood disaster. International Journal of Remote Sensing 40, 5050–5077.

Wang, Y., Colby, J. D., Mulcahy, K. A., 2002. An efficient method for mapping flood extent in a coastal floodplain using landsat tm and dem data 23, 3681–3696.

## List of Figures

1 Location of the study area (© University of Texas Libraries (left), and Thua Thien Hue Department of Tourism (right)). . . . . 6

2 Preprocessing chain for Sentinel-1 image time series. . . . . 8

3 Flowchart of the multiscale change analysis for SAR ITS. . . . . 9
4 A quadtree with four levels of decomposition. . . . . 10
5 SAR image split into tiles based on the quadtree decomposition. (a) Sentinel-1 SAR image of Thang Binh district, Quang Nam province, Vietnam, acquired on September 11, 2017, (b) Quadtree-based tiles of the image in Fig. 5a, (c) Final quadtree-based tiles of the time series. . . . . 12
6 Six types of changes can be observed by TCDMs. Left: temporal profiles; Right: TCDMs' appearances. (a), (b) Temporal stability; (c), (d) Chaotic change; (e), (f) Dirac change; (g), (h) Step change; (i), (j) Rampe change; (k), (l) Periodic change. . . . . 31
7 Map of change dynamics showing the frequency of all kinds of changes occurred in the study area. (1), (2), (3): three regions of interest; (a), (b), (c), (d), (e), (f), (g): locations of observed tiles in Fig. 8; (+): location of observed tile in Fig. 9 f. . . . . 32
8 TCDMs and temporal profiles at regions affected by floods. Left: TCDMs; Right: temporal profiles of tile stacks. (a), (h) Flood on November 10, 2017; (b), (i) Flood on November 22, 2017; (c), (j) Flood on December 11, 2018; (d), (k) Floods on November 10, 2017 and November 22, 2017; (e), (l) Floods on November 10, 2017 and December 11, 2018; (f), (m) Floods on November 22, 2017 and December 11, 2018; (g), (n) Floods on November 10, 2017, November 22, 2017 and December 11, 2018. . . . . 33
9 TCDMs and temporal profiles at several specific regions. Left: TCDMs; Right: temporal profiles of tile stacks. (a), (g) Rice field affected by three floods on November 10, 2017, November 22, 2017 and December 11, 2018; (b), (h) Rice field not affected by floods; (c), (i) Aquaculture lagoon affected by three floods on November 10, 2017, November 22, 2017 and December 11, 2018; (d), (j) Lake; (e), (k) Rocky mountain area with almost no change; (f), (l) A dirac change not caused by a flood. . . . . 34

10 Inundation map of the study area in two rainy seasons, from September to December of 2017 and 2018 (opened in Google Earth). . . . . 35

11 Accuracy assessment of flood detection. (a) Flood map of Thua Thien Hue province on November 7, 2017, regarding the typhoon Damrey, © Brakenridge and Kettner (2017) (Red: flooding mapped from NASA MODIS and Copernicus Sentinel-1 data, Gray: previously-mapped flooding, Blue: reference normal water extent); (b) Flood map of Thua Thien Hue province on November 10, 2017 produced by the proposed framework from Sentinel-1 data and comparison samples manually extracted from the map in Fig 11 a (White: flooded areas, Blue: flooded samples, Maroon: non-flooded samples, Green: false alarms, Red: missed alarms). . . . . 36

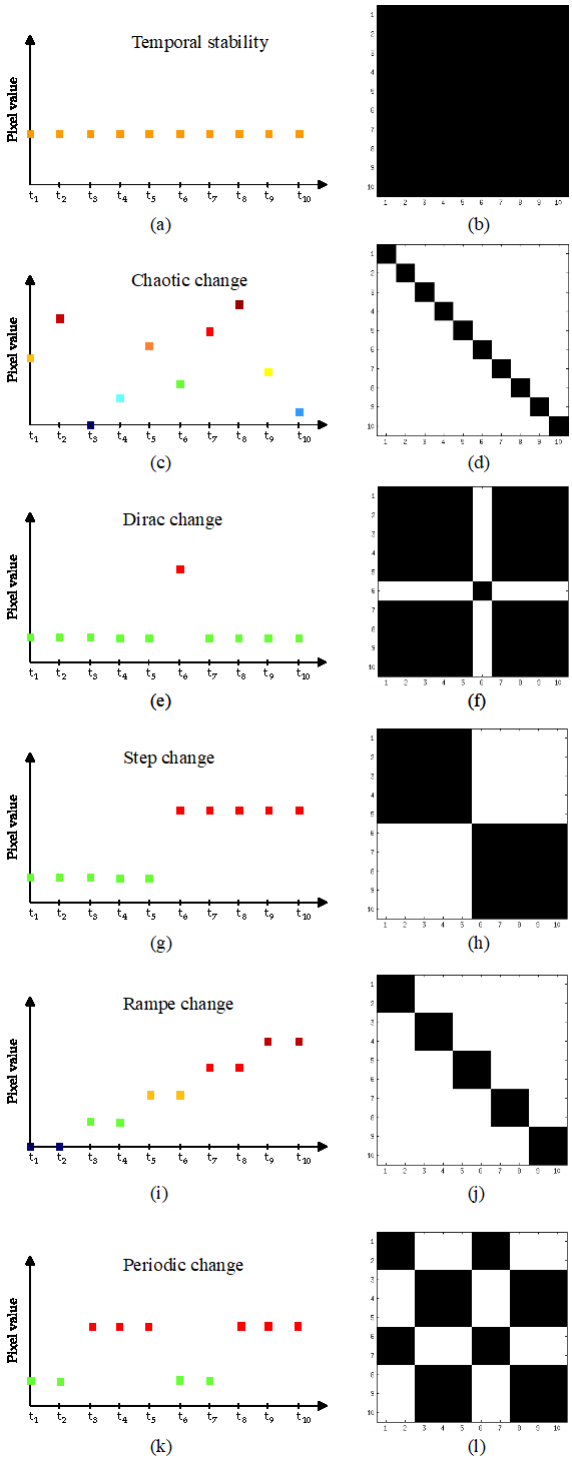


Figure 6: Six types of changes can be observed by TCDMs. Left: temporal profiles; Right: TCDMs' appearances. (a), (b) Temporal stability; (c), (d) Chaotic change; (e), (f) Dirac change; (g), (h) Step change; (i), (j) Rampe change; (k), (l) Periodic change.

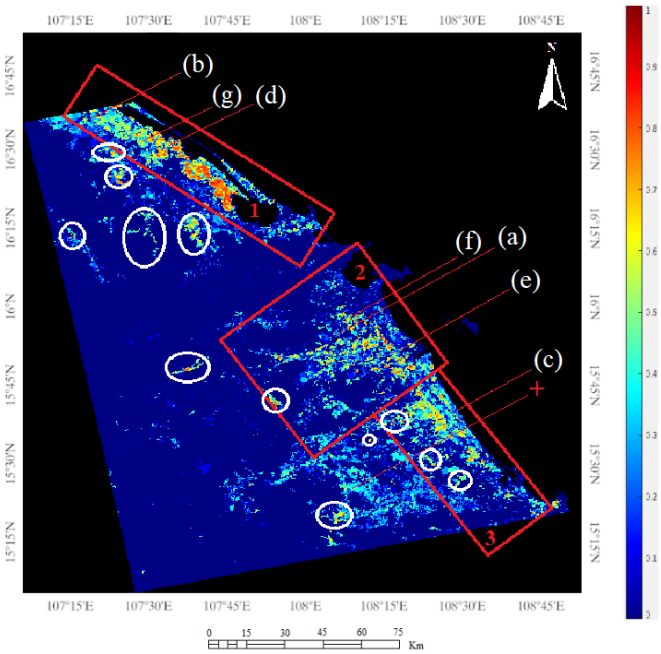


Figure 7: Map of change dynamics showing the frequency of all kinds of changes occurred in the study area. (1), (2), (3): three regions of interest; (a), (b), (c), (d), (e), (f), (g): locations of observed tiles in Fig. 8; (+): location of observed tile in Fig. 9 f.

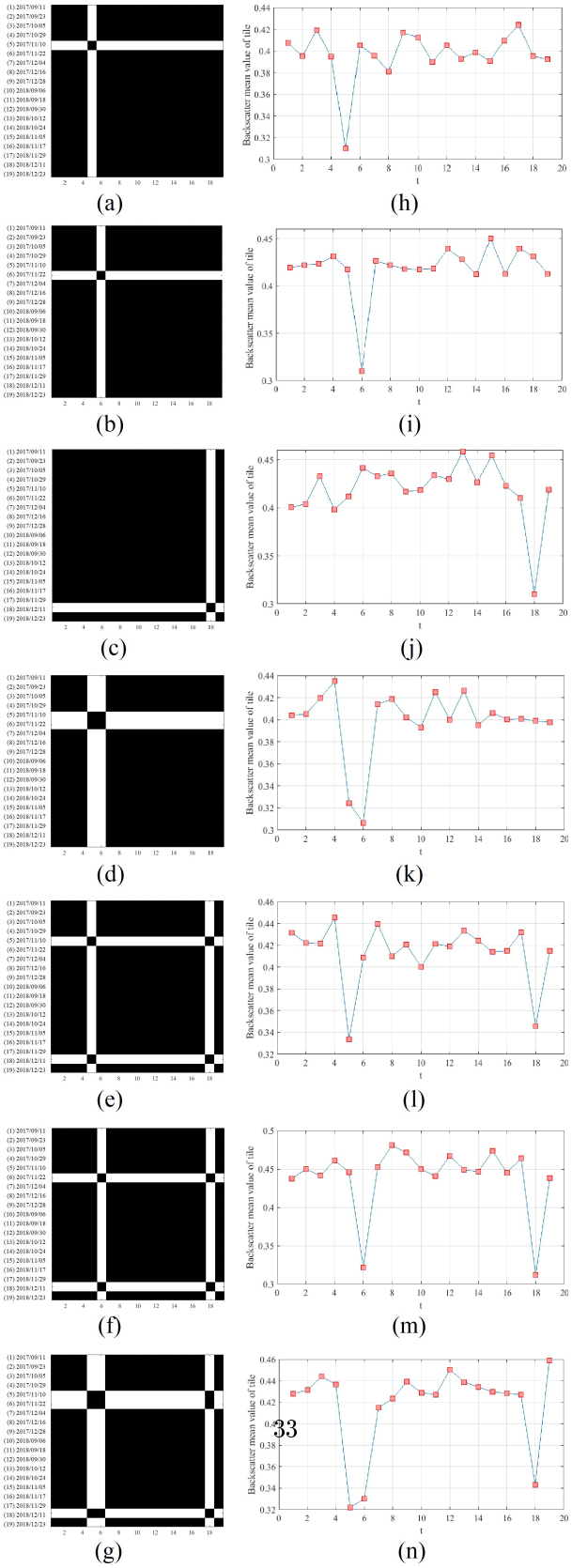


Figure 8: TCDMs and temporal profiles at regions affected by floods. Left: TCDMs; Right: temporal profiles of tile stacks. (a), (h) Flood on November 10, 2017; (b), (i) Flood on November 22, 2017; (c), (j) Flood on December 11, 2018; (d), (k) Floods on November 10, 2017 and November 22, 2017; (e), (l) Floods on November 10, 2017 and December 11, 2018; (f), (m) Floods on November 22, 2017 and December 11, 2018; (g), (n) Floods on November 10, 2017, November 22, 2017 and December 11, 2018.

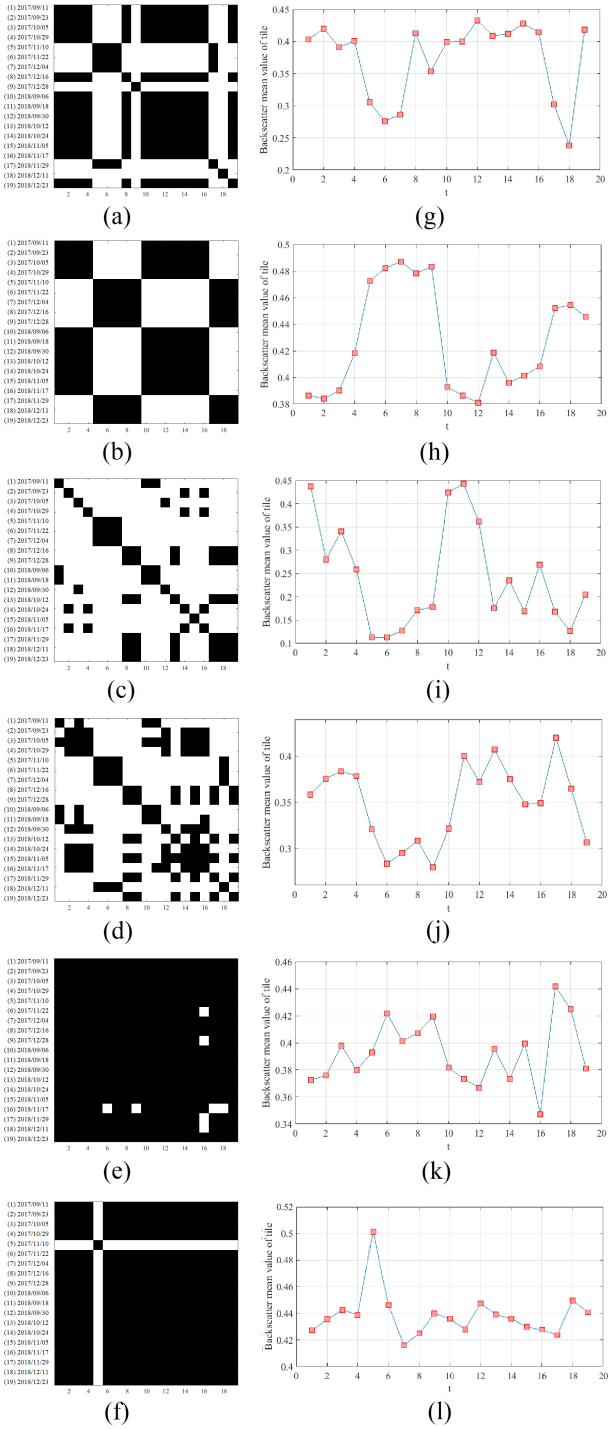


Figure 9: TCDMs and temporal profiles at several specific regions. Left: TCDMs; Right: temporal profiles of tile stacks. (a), (g) Rice field affected by three floods on November 10, 2017, November 22, 2017 and December 11, 2018; (b), (h) Rice field not affected by floods; (c), (i) Aquaculture lagoon affected by three floods on November 10, 2017, November 22, 2017 and December 11, 2018; (d), (j) Lake; (e), (k) Rocky mountain area with almost no change; (f), (l) A dirac change not caused by a flood.

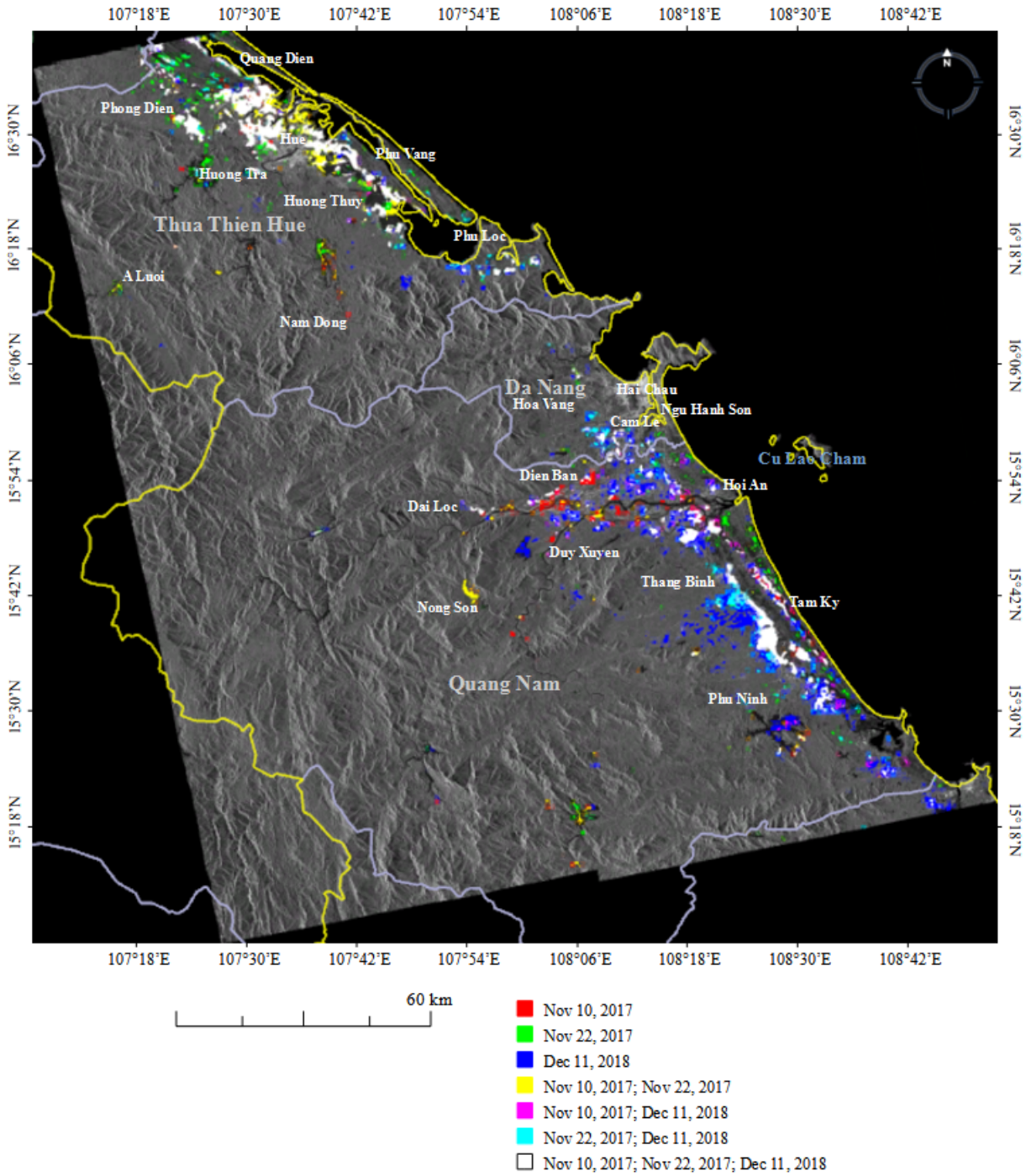


Figure 10: Inundation map of the study area in two rainy seasons, from September to December of 2017 and 2018 (opened in Google Earth).

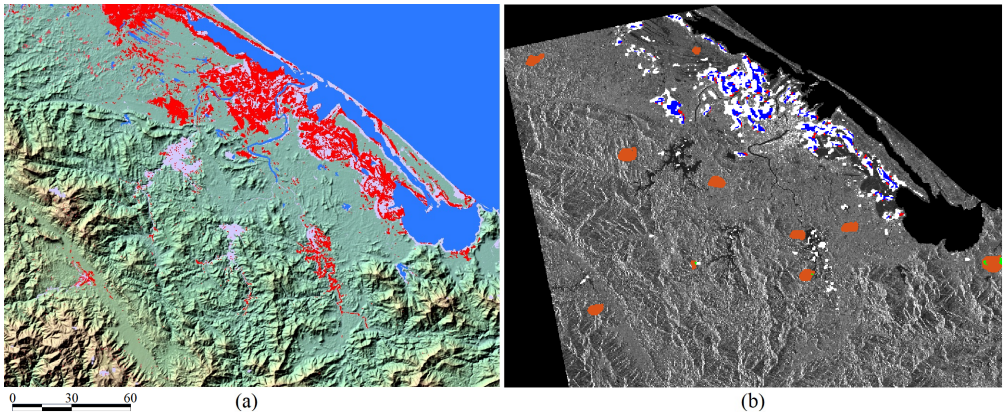


Figure 11: Accuracy assessment of flood detection. (a) Flood map of Thua Thien Hue province on November 7, 2017, regarding the typhoon Damrey, © Brakenridge and Kettner (2017) (Red: flooding mapped from NASA MODIS and Copernicus Sentinel-1 data, Gray: previously-mapped flooding, Blue: reference normal water extent); (b) Flood map of Thua Thien Hue province on November 10, 2017 produced by the proposed framework from Sentinel-1 data and comparison samples manually extracted from the map in Fig 11 a (White: flooded areas, Blue: flooded samples, Maroon: non-flooded samples, Green: false alarms, Red: missed alarms).